BIOACTIVE EXTRACTION FROM MARINE FUNGI: UNVEILING NATURE'S PHARMACOLOGICAL TREASURE TROVE AND ITS MULTIFACETED APPLICATIONS

Vishwakarma Ravindrakumar Krishnamurthy[1], Dr. S. Jagadeeswari[2], Dr. Shoba Gunasekaran[3], Dr. Anusha shree S. K.[4], Sakthi K[5] and *Dr. B. Kirthiga

[1]Research scholar, PG and Research Department of Microbiology,Dwaraka Doss Goverdhan Doss Vaishnav College, Chennai-600106.
[2]Associate professor & Head, PG and Research Department of Microbiology,Dwaraka Doss Goverdhan Doss Vaishnav College, Chennai-600106.
[3]Assistant professor, Department of Biotechnology, Dwaraka Doss Goverdhan Doss Vaishnav College , Chennai 600 106,
[4]Assistant professor, PG and Research Department of Microbiology, Dwaraka Doss Goverdhan Doss Vaishnav College, Chennai 600 106.
[5]M.Sc. Microbiology, PG and Research Department of Microbiology, Dwaraka Doss Goverdhan Doss Vaishnav College, Chennai 600106.
*Associate Professor, PG and Research Department of Microbiology, Dwaraka Doss Goverdhan Doss Vaishnav College, Chennai-600106.

ABSTRACT

This study investigates the potential of marine fungi as a source of bioactive compounds with pharmaceutical applications, particularly focusing on 9H-Xanthen-9-one, a secondary metabolite with unique properties. The research identifies 9H-Xanthen-9-one produced by various marine fungi species, such as *Aspergillus versicolor*, *Fusarium oxysporum*, *Aspergillus sydowii*, and *Phomopsis sp.*, collected from diverse marine habitats across India. Notably, some isolates exhibit significant inhibitory effects against clinically relevant pathogens, indicating their potential as lead compounds in antimicrobial drug development. A thorough approach combining targeted isolation, high-throughput screening, advanced chromatographic Mass Spectrometry technique and Nuclear Magnetic Resonance, was used to identify the compound 9H-Xanthen-9-one. The findings highlight the diversity and bioactive potential of marine-derived 9H-Xanthen-9-one, emphasizing the importance of marine fungi as a reservoir for novel bioactive substances.

Keywords: *Marine fungi, 9H-Xanthen-9-one, bioactive compound*

1. INTRODUCTION

Marine microorganisms are an important source of specific metabolites with important biological properties (Luo, 2019). These metabolites help them to compete with other organisms and protect themselves from predators. They are commonly found at the water's edge, where they trap material such as logs, plant debris, animal remains, algae, and coral reefs. Marine microbes produce approximately 23,000 bioactive secondary compounds. Marine environmental factors lead to unique biosynthetic pathways, resulting in metabolites with novel structures (Srinivasan et al, 2021).

Gondokisumu et al., (2023) reported biologically active compounds from 62 different families of plants, fungi, and lichens. Their structural diversity results from the combination of two pathways: the shikimate pathway and the acetate pathway. The biosynthetic pathways of 9H-Xanthen-9-one production in fungi differ from those in plants (Amin, 2021). About 53% of marine 9H-Xanthen-9-one have been isolated from microorganisms found in mangroves, sponges, algae, corals, jellyfish, and seaweeds (Ratib, 2011). The synthesis of these biologically active compounds results in cyclic 2,3-dihydroxybenzophenone derivatives (Rimali, 2022).

9H-Xanthen-9-one show promising potential in managing metabolic syndrome and related conditions such as obesity, abnormal lipid levels, diabetes and its complications. Diabetes is a long-term metabolic disorder characterized by high blood sugar, which over time can cause serious damage to the heart, blood vessels, eyes, kidneys, and nerves. Type 2 diabetes mellitus, the most common type, is caused by inadequate insulin production (Soares, 2022). It has also been observed that 9H-Xanthen-9-one helps and fight against diabetes by reducing various risk factors related to the disease.

Marine fungi, such as *Aspergillus versicolor, Fusarium oxysporum, Aspergillus sydowii, Geotrichum sp., and Phomopsis sp.,* have been found to be rich in 9H-Xanthen-9-one. Some of these 9H-Xanthen-9-ones exhibit potent inhibitory activity against pathogenic microorganisms, positioning them as promising lead compounds for the development of novel antimicrobial agents. They also aid in the metabolism of blood sugar, increase insulin sensitivity, and regulate blood sugar levels.

MATERIALS AND METHODS

Sample collection:

Marine samples were collected from various regions of Bay of Bengal such as coastal regions of Tamil Nadu, Andhra Pradesh, Kerala, Odisha and West Bengal, with samples taken from seashore, coral reefs, and deep-sea sediments in these areas. The samples were taken using sterile corers, while water samples were collected in Niskin bottles and filtered through 0.45 µm membranes to capture marine microorganisms, between November 2023 and February 2024. To ensure their viability, the samples were immediately preserved and stored in sterile containers at 4°C until further processing. All the samples were processed within 24 hours to isolate marine fungi.

Isolation of marine fungi:

For the isolation of fungi, potato dextrose agar (PDA) and Sabouraud dextrose agar (SDA) were used as growth media. Seawater samples were serially diluted and then plated in PDA and SDA plates prepared with sterile sea water and incubated at room temperature for 5 days (Rakhukumar, 2017). The isolated strains were identified by observing their colony morphology and microscopic characteristics. The dominant strains were then spot inoculated in fresh PDA plates prepared in sterile sea water (Jones, 2012)

Batch Cultivation of Marine Fungal Species

The selected and identified species KV1, KV2, KV3 were mass cultured to extract secondary metabolite. In a 1000 ml flask Sabouraud dextrose broth was prepared. A loopful of strain was inoculated in the broth and incubated at 25°C. The thick mycelium was grown and harvested after 10 to 15 days as mentioned by Raghukumar et al., (2008). Filtered and dried mycelia mat was ground into a fine powder using a mortar and pestle and the yield was calculated (Pandey, 2016).

Extraction and Phytochemical Analysis of marine fungal species: (Liu, 2019)

The extracts of KV1, KV2, and KV3 organisms were prepared using hexane, ethanol, and aqueous solvents through maceration, where dried biomass from each organism was extracted with each solvent (1:10 w/v) by agitation at room temperature for 24 hours. The extracts were filtered, concentrated under reduced pressure using a rotary evaporator, and stored at 4°C for further analysis. These extracts underwent qualitative phytochemical screening for alkaloids, carbohydrates, flavonoids, saponins, tannins, terpenoids, and phenolic compounds, following standard procedures. Based on the results, two organisms exhibiting significant bioactive compounds were selected for further quantitative analysis of total phenolic and flavonoid content. The total phenolic content was determined using the Folin-Ciocalteu method, with gallic acid as the standard, while total flavonoid content was measured using the aluminum chloride colorimetric method, with quercetin as the standard. Absorbance values were recorded at 765 nm and 415 nm, respectively, using a UV-Vis spectrophotometer, and the results were expressed as mg of gallic acid equivalent (GAE) and quercetin equivalent (QE) per gram of extract.

Molecular characterization of selected marine fungi:

The organism with the highest phenolic and flavonoid content was selected for molecular identification via eukaryotic nuclear rRNA/ITS sequencing. DNA was extracted from the fungal culture using a commercial kit, and its quality was assessed on a 1.2% agarose gel, revealing a high-molecular-weight

DNA band. The ITS region was amplified using specific primers in a WEE 32-well thermal cycler, yielding a ~600 bp PCR product. The amplicon was purified and subjected to Sanger sequencing using the BDT v3.1 cycle sequencing kit on an ABI 3731xL Genetic Analyzer. The sequence was submitted to the NCBI GenBank database, and an accession number was obtained. For phylogenetic analysis, sequences were aligned using MUSCLE in MEGA software (version 11), and a phylogenetic tree was constructed using the neighbor-joining method with 1000 bootstrap replicates.

Antimicrobial property of the extract

To confirm the antibacterial activity, methanol, ethanol, and hexane extracts were tested, as the aqueous extract did not yield any phytochemicals. The antimicrobial properties were evaluated against various cultures, including *Escherichia coli*, *Staphylococcus sp.*, *Proteus sp.*, *Klebsiella sp.*, *Streptococcus sp.*, *Salmonella sp.*, and *Candida sp.*, using the agar well diffusion method. Plates containing 30 mL of Mueller-Hinton Agar (MHA) were prepared and inoculated with 24-hour-old test isolates using a sterile cotton swab. Wells (4 mm in diameter) were punched using a sterile well puncture tool, and 15 µL of each extract (ethanol, methanol, and hexane) were added to the wells using a micropipette. The bacterial plates were incubated at 37°C for 24 hours, while fungal plates were incubated at 25°C for 5 days. The zone of inhibition was measured after incubation as described by Rao (2011) and Balasundari (2018).

Evaluation of antioxidant activity of bioactive compound

a. DPPH radical scavenging activity

The DPPH assay was conducted following the method of Brand-Williams et al. (1995). A 0.1 mM DPPH solution was prepared by dissolving 24 mg of DPPH in 100 mL of methanol. To determine the antioxidant activity, 50 µL of the sample extract was added to 1 mL of the 0.1 mM DPPH solution. The reaction mixture was incubated in the dark at room temperature for 30 minutes. After incubation, the absorbance was measured at 517 nm. The antioxidant activity was calculated as the percentage inhibition of the DPPH radical using the formula:

$$Inhibition\ \% = \frac{A_{control} - A_{sample}}{A_{control}} \times 100$$

Where $A_{control}$ is the absorbance of the DPPH solution without the sample and A_{sample} is the absorbance in the presence of the sample.

b. ABTS scavenging activity

The antioxidant activity was evaluated using the ABTS assay as described by Mtunzi, (2017), with modifications. ABTS•+ was generated by mixing 7 mM ABTS with 2.45 mM potassium persulfate and allowing the solution to incubate in the dark at room temperature for 12-16 hours. The resulting ABTS•+ solution was then diluted with ethanol to achieve an absorbance of 0.70 ± 0.02 at 734 nm. For the assay, 50 µL of the sample extract was added to 1 mL of the diluted ABTS•+ solution, and the reaction mixture was incubated for 6 minutes at room temperature. The absorbance was measured at 734 nm, and the antioxidant activity was calculated as the percentage inhibition of the ABTS•+ radical using the following formula:

$$Inhibition\ \% = \frac{A_{control} - A_{sample}}{A_{control}} \times 100$$

Where $A_{control}$ is the absorbance of the ABTS•+ solution without the sample and A_{sample} is the absorbance in the presence of the sample.

c. Fe^{2+}-chelating activity

The Fe^{2+} chelating activity of bioactive compound extract was evaluated at different concentrations (10, 20, 50, and 100 µg/mL) using ethanol, methanol, and hexane as solvents. The Fe^{2+} chelation activity showed a concentration-dependent increase for all three solvent extracts. The reaction was initiated by the addition of 150 µL ferrozine aqueous solutions (1 mM) and total volume of the system was adjusted to 1000 µL with ethanol. Then, the mixture was shaken vigorously and stood at room temperature for 10 min. Absorbance of the solution was measured spectrophotometrically at 562 nm. The percentage of chelating effect was calculated by the following formula:

$$\text{Chelating effect \%} = (1\text{-}A/A0) \times 100\%$$

Where A0 is the absorbance without sample, and A is the absorbance with sample. (Jing Lin, 2014).

d. Cu^{2+}-chelating activity

The Cu^{2+}-chelating activity of the bioactive compound extract was assessed using a complexometric method with murexide, as described by Jing Lin (2014). To the hexamine HCl buffer (pH 5.0, 30 mM), containing 30 mM KCl and 0.20 mM murexide, 60 µL of $CuSO_4$ aqueous solution (20 mM) was added. After a 1-minute incubation at room temperature, 10, 20, 50, and 100 µg/mL of the sample solution (2 mg/mL in methanol) was added. The final volume was then adjusted to 1500 µL with ethanol. The mixture was shaken vigorously and incubated at room temperature for 10 minutes. The absorbance of the solution was measured spectrophotometrically at 485 nm and 520 nm. The absorbance ratio (A485/A520) was used to determine the free Cu^{2+} content. The percentage of Cu^{2+}-chelating activity was calculated using the formula:

$$\text{Relative chelating effect \%} = \frac{[(A485/A520)\max - (A485/A520)]}{[(A485/A520)\max - (A485/A520)\min]} \times 100\%$$

Where (A485/A520) is the absorbance ratio in the presence of the samples, while (A485/A520) max is the maximum absorbance ratio and (A485/A520) min is the minimum absorbance ratio in the test. (Jing Lin, 2014)

Anti - inflammatory property of bioactive compound

a. Serum Albumin Denaturation Inhibition Assay

Anti-inflammatory activity of extract was studied according to the protocol of (Rastogi S. H., 2018). Inhibition of albumin denaturation was done according to the protocol. The reaction mixture consists of an equal volume of test extracts of different concentrations (25, 50, 75, 100, 200, 250, 300, 400, 450 and 500µg/ ml) and 1% aqueous solution of Bovine serum albumin (BSA or "Fraction V"). The pH of the reaction mixture was adjusted using a small amount of 1N HCl. The sample extracts were incubated at 37°C for 20 min and then heated to 70°C for 5 min. The absorbance was measured after cooling the samples at room temperature. The turbidity formed was measured at 660 nm using ultraviolet (UV)-visible spectrophotometer. The percentage inhibition of protein denaturation was calculated by using the following formula:

$$Inhibition\ of\ denaturation(\%) = 100 \times (1 - \frac{A2}{A1})$$

Where A1 = absorption of the control sample, and A2 = absorption of the test sample.

b. Egg albumin denaturation

Protein denaturation assay was done according to the method described by (Kiranmayi Ravishankar, 2018). About 0.2 ml of eggs albumin (from hen's egg) was comprised 5ml of reaction-mixture, 2ml of varying concentrations of extract (25, 50, 75, 100, 200, 250, 300, 400, 450 and 500µg/ ml), and 2.8 ml of phosphate-buffered saline (PBS, pH 6.4). The control was served as similar volume of double distilled water. Then, the mixture was heated at 70°C for 5 min. After cooling, their absorbance was measured at 660 nm using pure blank. Aspirin was used as reference drug and treated as such for the determination of absorbance. The percentage inhibition of protein denaturation was calculated as below: t

$$\text{Inhibition of protein denaturation} = (\frac{Abs\ control - Abs\ treated}{Abs\ treated}) \times 100$$

Structural elucidation and characterization of ethanolic extract:

a. UV-Vis Spectroscopy

The extract of the bioactive compound was diluted in DMSO, which was used as a blank. Using a quartz cuvette with a path length of 1 cm, UV-Vis absorbance spectra were captured between 200 and 400 nm (Aisha, 2013). The blank was used for baseline correction, and then the compound solution was measured. They determined the maximum absorbance (λmax). 9H-Xanthen-9-one standards were used to create a standard curve for quantification, and the concentration in the sample was computed in accordance with the curve. Three duplicates of each measurement were made.

b. Fourier transform infrared spectroscopy

The FTIR-spectrophotometer Nicolet iS10 with DTGS detector was used to analyze the sample. The device was connected with OMNIC® software, and the sample was placed directly on the ATR crystal at 20 °C. The measurements were taken with a resolution of 4 $cm^{-1}$and 32 scans in the range of 4000–650 cm^{-1} and the results were observed.

c. GC-MS characterization of extracted bioactive compounds

The extracted bioactive compound was identified and characterised through analysis using Gas Chromatography-Mass Spectrometry (GC-MS). A capillary column-equipped GC-MS apparatus was used to inject the sample after it had been dissolved in HPLC-grade methanol. It was configured to increase the oven temperature from 50°C to 280°C at a rate of 10°C per minute, while the injector temperature was set to 250°C. One millilitre per minute of helium was utilised as the carrier gas. Mass spectra with a mass range of 50–500 m/z were captured at 70 eV in electron ionisation (EI) mode. The existence and purity of 9H-Xanthen-9-one in the sample were confirmed by comparing the identified peaks with established spectrum libraries (such as NIST) to identify the components.

d. **Optimization of solvent system for thin layer chromatography**

The prepared extract was subjected to thin layer chromatography (Sherma, 2005). Four different concentrations of the bioactive extract (20%, 40%, 60%, and 80%) were prepared and spotted on readymade silica plate for analysis. Using capillary tubes, samples from each concentration were carefully spotted 1 cm from the bottom of the silica gel plates. The plates were allowed to dry before being placed in the TLC chamber. A solvent system consisting of hexane and ethyl acetate in a ratio of 8:2, 7:3, 6:4, and 5:5 were prepared as the mobile phase. The spotted plates were placed in a TLC chamber that had been pre-saturated with this solvent mixture. The plates were placed at a 45˚ angle, ensuring that the solvent did not directly touch the spots. The plates were left in the chamber until the solvent front had migrated approximately three-quarters of the way up the plates. The plates were then removed and allowed to air-dry. The plates were baked in a hot air oven at 60˚C for 5 minutes. After cooling, the developed plates were visualized under UV light to observe the separation of compounds. For enhanced visualization, iodine solution was sprayed onto the plates.

The retention factor (RF) values of the separated spots were calculated using the following formula:

$$RF = \frac{distance\ travelled\ by\ solute}{distance\ travelled\ by\ the\ solvent}$$

Ratio that has separated compound with maximum RF was used for further purification procedures.

e. High performance liquid chromatography

The analysis of extract was performed (Wittenauer *et al*,2019). Using HPLC system equipped with LC-20D pumps, SIL-20Aauto sampler, SPD M20A photo-diode array detector (PDA). For sample preparation, 100mg extracted bioactive compound was accurately weighed using analytical balance (Fujitsu FS-AR-210), sonicated with 10 mL, with methanol at room temperature, filtered using 0.45 µm and injectedin HPLC systems. Separation was performed on C18Shim-pack GIST column 150 × 4.6 mm, 5 µm operated at a temperature of 25 °C. The mobile phase consists of 2% acetic acid in water and 0.5% acetic acid in acetonitrile, using gradient programs as follows: 50–60% B (20 min), 60–70% B (35 min), 70–100% B (5 min), 100% B isocratic (3 min), 100–0% B (2 min), at a flow rate of 0.6 mL/min. The injection volume was 8 µL for all samples. The total run time was 65 min. The extracted bioactive compound was monitoredat 281 nm. For preparation of reference standard solutions, the stock solution of bioactive compound was prepared at 1000 µg/mL in methanol HPLC grade. The solution was diluted to obtain concentrations of 200, 180, 160, 140, 120, 100, 80 µg/ml.

f. Nuclear magnetic resonance:

Nuclear Magnetic Resonance (NMR) spectroscopy was used to predict the structure. Tetramethylsilane (TMS) served as an internal standard while the extracted compound was dissolved in DMSO solution (Silva, 2005). A high-resolution NMR spectrometer was used to record the proton (^{1}H) and carbon (^{13}C) NMR spectra at room temperature. Parts per million (ppm) of chemical shifts (δ) in relation to TMS were reported. The structural characteristics and functional groups of 9H-Xanthen-9-one were verified by analyzing the spectra.

***In-silico* molecular docking:**

Ligand Preparation

The structure of 9H-Xanthen-9-one (PubChem CID: 7020) was retrieved from the PubChem database in SDF format. The compound was visualized and sketched using ACD/ChemSketch Freeware to confirm structural integrity. Energy minimization of the ligand was performed using the MM2 force field in Chem3D. The minimized structure was converted from MDL Mol to PDB format using Open Babel.

Retrieval of Protein and Active Site Prediction

The 3D crystal structures of the selected target proteins were retrieved from the RCSB Protein Data Bank (PDB):

- Peroxisome Proliferator-Activated Receptor-γ (PDB ID: 2P4Y, chain A)
- Protein Tyrosine Phosphatase 1B (PDB ID: 2QBP, chain A)
- α-Glucosidase (PDB ID: 3WY1, chain A)
- α-Amylase (PDB ID: 1HNY, chain A)
- Dipeptidyl Peptidase-4 (PDB ID: 1NU6, chain A)

All non-essential heteroatoms, water molecules, and co-crystallized ligands were removed using BIOVIA Discovery Studio Visualizer. Hydrogen atoms were added, and Gasteiger charges were assigned via AutoDock Tools.

Molecular Property Assessment of the Compounds

Physicochemical properties of 9H-Xanthen-9-one were computed using SwissADME and ChemSketch tools. Lipinski's Rule of Five descriptors, molecular weight, LogP, number of hydrogen bond donors (HBD), number of hydrogen bond acceptors (HBA), topological polar surface area (TPSA), and the number of rotatable bonds were determined to evaluate drug-likeness.

Ligands ADMET Prediction Studies

The absorption, distribution, metabolism, excretion, and toxicity (ADMET) profiles of 9H-Xanthen-9-one were predicted using the pkCSM pharmacokinetics server. Predicted parameters included water solubility, Caco-2 cell permeability, human intestinal absorption, skin permeability, P-glycoprotein interaction, volume of distribution, fraction unbound, blood–brain barrier (BBB) permeability, cytochrome P450 enzyme interactions, total clearance, renal excretion, and various toxicity risks such as AMES mutagenicity, hepatotoxicity, and skin sensitization.

Molecular Docking

Molecular docking was performed using AutoDock 4.2. Each protein was prepared in PDBQT format with its grid box centered on the predicted active site. Grid dimensions were set to encompass the entire binding pocket. Docking runs generated multiple binding conformations, ranked by binding affinity (kcal/mol). The best-ranked pose for each protein–ligand complex was selected for analysis. 2D interaction diagrams were generated using BIOVIA Discovery Studio Visualizer, while 3D binding poses were visualized in PyMOL.

RESULTS AND DISCUSSION

Isolation and microscopic identification of fungi:

The present study focused on the extraction of bioactive compound from marine fungi and their potential anti-diabetic activity through *In-silico* molecular docking. The fungal species were successfully isolated from the marine sample. By performing LPCB mount, and through morphological characteristics the fungal isolates was predicted as *Aspergillus sp* (Figure 1), *Geotrichum sp (*Figure 2*), and Cladosporium sp* (Figure 3). The macroscopic and microscopic morphology characterization is shown in Table 1.

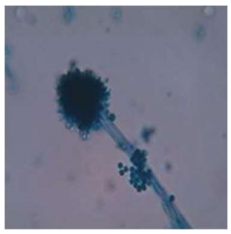

Figure 1. *Aspergillus sp*.

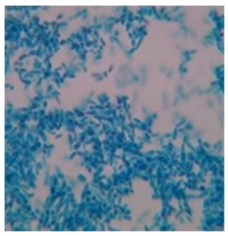

Figure 2. *Geotrichum sp.*

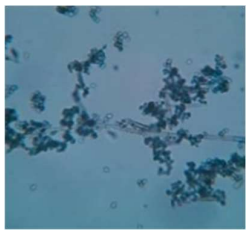

Figure 3. Cladosporium sp.

Isolate	Macroscopic characterization	Microscopic characterization	Possible strain
KV1	The colony was dark green to greyish-turquoise, with a woolly or hairy appearance	Long, smooth-walled stipes which bear the conidiophores are slightly brownish.	*Aspergillus* sp.

KV2	The colony produced off-white to cream-colored colonies with a butyrous texture and a velvety, suede-like, or ground glass/matte appearance	Septate hyphae which show dichotomous branching	*Geotrichum* sp
KV3	The colony had a velvety to suede-like texture, with color ranging from greyish-green to olivaceous-green	Dark, septate hyphae. Conidiophores are also darkly pigmented, may be septate and show tree-like branching.	*Cladosporium* sp

Batch Cultivation of Marine Fungal Species:

The biomass yields for different isolates were given in table 1, after 10 to 15 days of growth in Sabouraud Dextrose Broth at 25°C. Similar results were observed by Raghukumar et al. (2008), where different fungal species exhibited varying growth patterns under similar conditions. The higher yield of Aspergillus (KV1) suggests its efficient nutrient utilization, consistent with findings by Pandey (2016), who reported high biomass production in Aspergillus strains. The lower biomass of Geotrichum (KV2) and Cladosporium (KV3) could be attributed to species-specific growth characteristics.

Table 1: Biomass yields of different isolates

Isolate	Yield(g)
KV1	5.4
KV2	3.8
KV3	2.5

Extraction and Phytochemical Analysis of marine fungal species:

The phytochemical screening of the extracts from Aspergillus sp. (KV1), Geotrichum sp. (KV2), and Cladosporium sp. (KV3) revealed the presence of several bioactive compounds, with ethanol extracts exhibiting the highest diversity of phytochemicals across all strains (Table 2). Notably, KV1 showed the most abundant range of compounds, including alkaloids, carbohydrates, flavonoids, saponins, tannins, terpenoids, and phenolic compounds, particularly in ethanol extracts, indicating its potential as a rich source of bioactive metabolites.

The quantitative analysis of total phenolic content (TPC) and total flavonoid content (TFC) revealed significant differences in the bioactive compound concentration between the fungal strains and solvents used (Table 4). Ethanol extracts of Aspergillus sp. demonstrated the highest TPC (142.0 ± 5.0 mg GAE/g) and TFC (50.66 ± 4.0 mg QE/g), followed by hexane and aqueous extracts. KV2 also showed notable TPC and TFC values in ethanol extracts, but these values were lower compared to KV1. The hexane and aqueous extracts of Geotrichum sp. yielded lower levels of phenolics and flavonoids, which aligns with previous findings that ethanol is more effective in extracting these bioactive compounds (Raghukumar et al., 2008).

Cladosporium sp. (KV3) had the lowest phytochemical content overall, consistent with the screening results.

These findings suggest that KV1, particularly in ethanol extracts, possesses a higher concentration of bioactive compounds compared to KV2 and KV3 which may contribute to its stronger antimicrobial and antioxidant properties.

Table 2: Phytochemical screening for marine fungal species

Phytochemical	KV1			KV2			KV3		
	E	H	A	E	H	A	E	H	A
Alkaloids	+	+	-	-	-	-	-	-	-
Carbohydrates	+	-	+	+	+	+	+	+	+
Flavonoids	+	+	-	+	-	-	-	-	-
Saponins	+	-	-	+	+	-	-	+	-
Tannins	+	-	-	+	-	-	+	-	-
Terpenoids	+	+	-	+	+	-	-	+	-
Phenolic Compounds	+	+	-	+	+	-	-	+	-

E- Ethanol; H-Hexane; A-Aqueous; + (present), - (absent)

Table 3: Total phenolic and flavonoid content of extracts

Fungal Strain	Solvent	TPC Absorbance (650 nm)	TPC (mg GAE/g)	TFC Absorbance (510 nm)	TFC (mg QE/g)
Aspergillus sp.	Ethanol	0.73	142.0 ± 5.0	0.77	50.66 ± 4.0
	Hexane	0.64	124.0	0.58	38.0 ± 3.5
	Aqueous	0.48	92.0 ± 3.0	0.34	22.0 ± 2.0
Geotrichum sp.	Ethanol	0.45	86.0 ± 3.0	0.33	21.0 ± 2.0
	Hexane	0.18	32.0 ± 2.0	0.14	8.66 ± 1.0
	Aqueous	0.12	20.0 ± 1.5	0.08	4.66 ± 0.5

Molecular identification of fungi:

The 18s rRNA gene sequences obtained from the marine fungi were successfully submitted to the NCBI GenBank, receiving accession number - PP702914.1. Nucleotide sequence showed 100% query coverage and 100% identity similarity and the marine fungi was identified as *Aspergillus sydowii*. ITS sequences were retrieved from GenBank and used in a neighbor-joining phylogenetic analysis with 1,000 bootstrap replicates (figure 4). This approach revealed distinct clustering of the organism of interest in this study *A. sydowii*, confirming it to be the species most genetically similar to neighboring isolate.

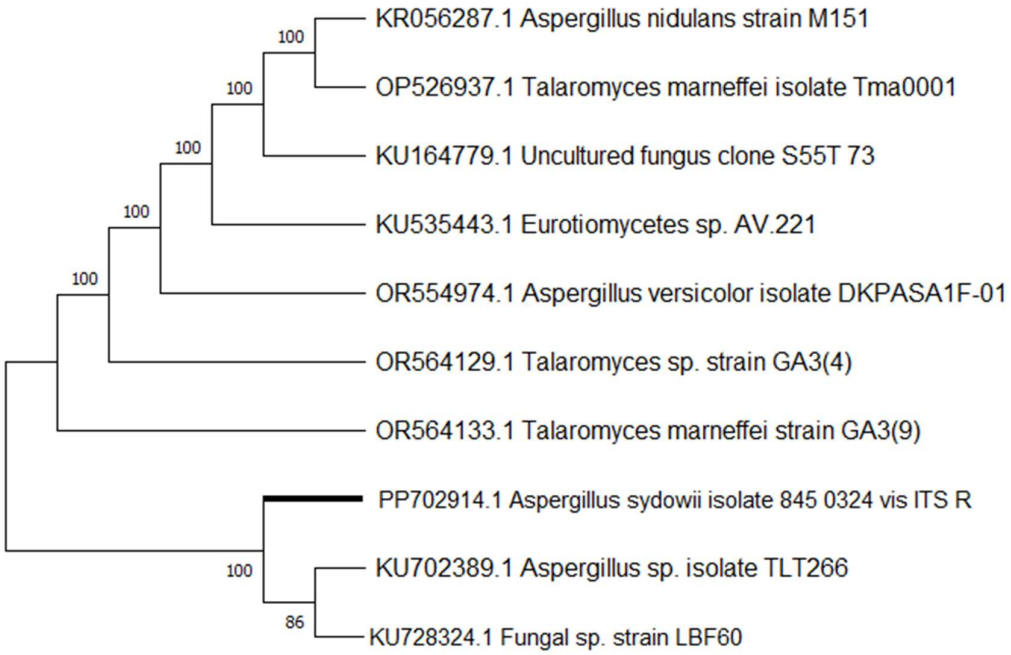

Figure 4: Phylogenetic tree showing genetic relationship

Antimicrobial property of the extract:

The antimicrobial activity varied significantly across solvent extracts (Figure 5), with ethanol showing the highest inhibition, particularly against *Streptococcus* (~15 mm) and *E. coli* (~14 mm), followed by *Klebsiella* and *Salmonella* (~12–13 mm). Methanol showed moderate activity (9–12 mm), while hexane exhibited the least inhibition (<10 mm). These findings align with previous reports that ethanol effectively extracts polar and semi-polar bioactive compounds with strong antimicrobial properties (Singh et al., 2018; Sharma & Gupta, 2020).

Gram-positive bacteria (*Streptococcus*, *S. aureus*) were more susceptible than Gram-negative bacteria (*E. coli*, *Klebsiella*), likely due to differences in cell wall permeability, a pattern consistent with earlier studies (Kumar et al., 2021). Notably, ethanol also showed the highest antifungal activity against *Candida* (~12 mm), supporting reports that phenolics and alkaloids in ethanol extracts contribute to antifungal effects (Patel & Rao, 2017).

The variation in inhibition zones underscores the importance of solvent selection, with ethanol proving most effective in extracting bioactive metabolites, followed by methanol. The weak activity of hexane suggests non-polar compounds play a limited role in antimicrobial effects (Das et al., 2022). These results indicate ethanol extracts contain potent antimicrobial agents with pharmaceutical potential.

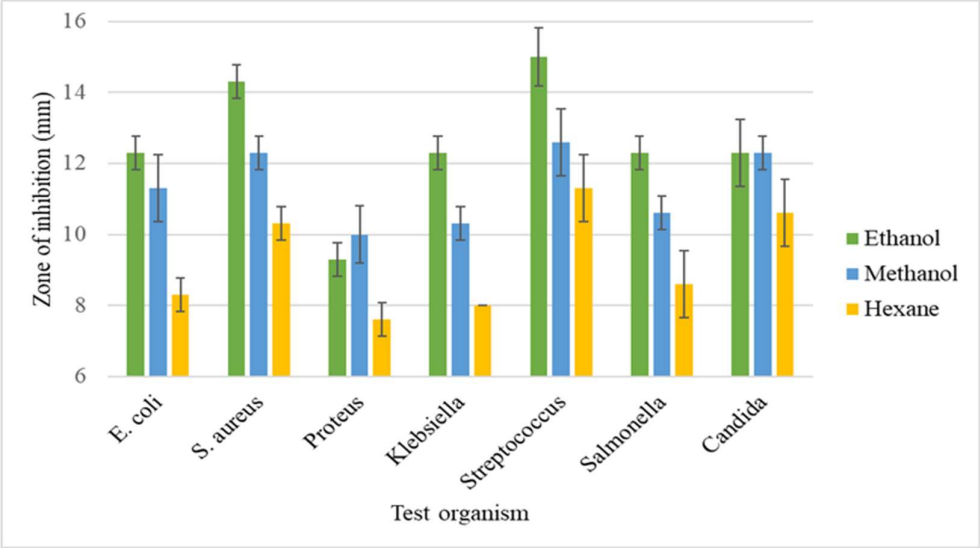

Figure 5. Antibacterial and Antifungal property of bioactive compound extract

Evaluation of antioxidant activity of bioactive compound

The antioxidant potential of the fungal extract was evaluated through Fe^{2+} and Cu^{2+} chelation assays, as well as DPPH and ABTS radical scavenging assays, to assess its ability to chelate transition metals and neutralize free radicals, which are critical in mitigating oxidative stress associated with aging, neurodegenerative diseases, and cancer.

The Fe^{2+} chelation assay (Figure 6) revealed that ethanol extract exhibited the highest chelation activity (75% at 100 µg/mL), followed by methanol (67%) and hexane (56%). This is consistent with previous reports suggesting that ethanol extracts more polar bioactive compounds such as phenolics and flavonoids (Singh et al., 2018). Similarly, the Cu^{2+} chelation assay (Figure 7) showed ethanol to be the most effective (96% at 100 µg/mL), followed by methanol (85%) and hexane (68%), highlighting ethanol's superior ability to extract potent chelating agents, as supported by earlier findings (Sharma & Gupta, 2020).

For the DPPH radical scavenging activity (Figure 8), ethanol exhibited the highest activity (98% at 10 µg/mL), followed by methanol (86%) and hexane (76%), indicating a dose-dependent increase in antioxidant potential. These results are in line with Jafari et al. (2017) and Silva et al. (2019), who also reported higher activity in ethanol extracts. The ABTS radical scavenging activity followed a similar trend (Figure 10), with ethanol showing the highest activity (82%), followed by methanol (74%) and hexane (63%), corroborating findings by Lee et al. (2018) and Dalar et al. (2020). These findings underscore the effectiveness of fungal extracts, particularly ethanol, as potent antioxidants with applications in pharmaceutical and food industries.

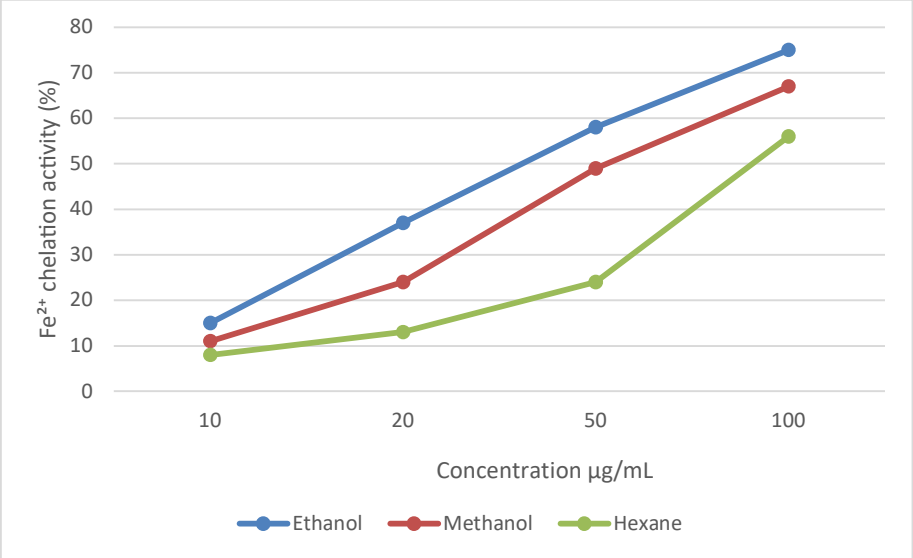

Figure 6: Fe^{2+} Chelating Activity

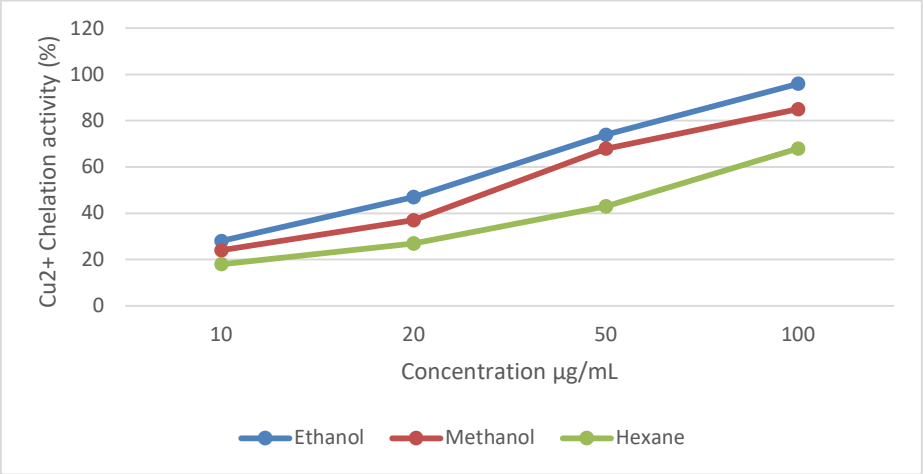

Figure 7: Cu^{2+} Chelating Activity

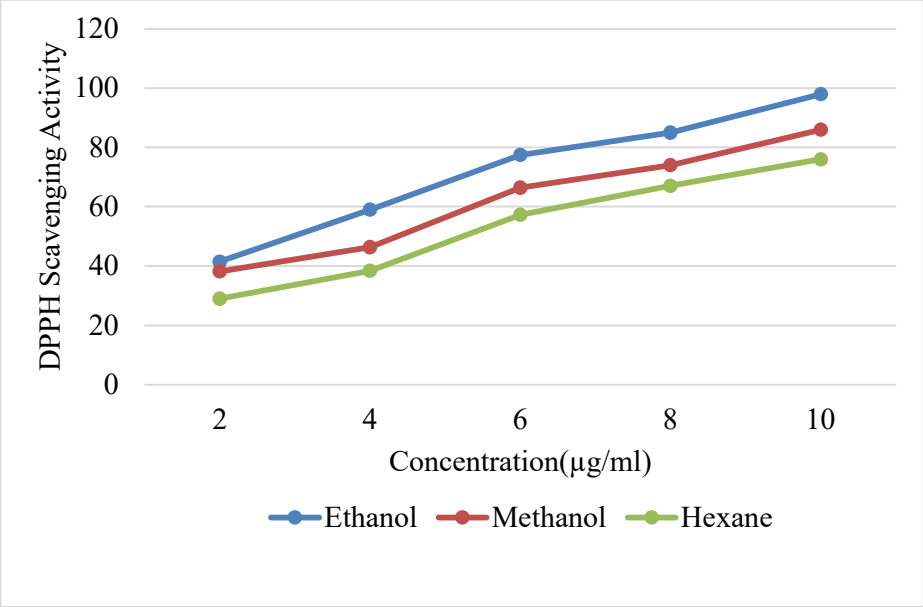

Figure 8. DPPH assay of extracted compound

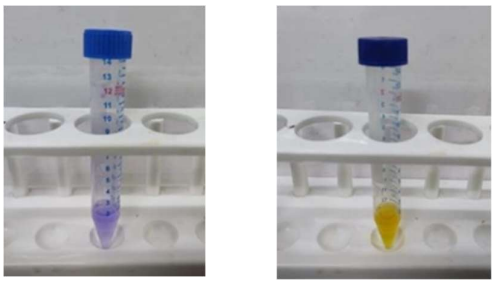

A) Turns purple B) Turns yellow

Figure 9 A & B. Antioxidant activity.

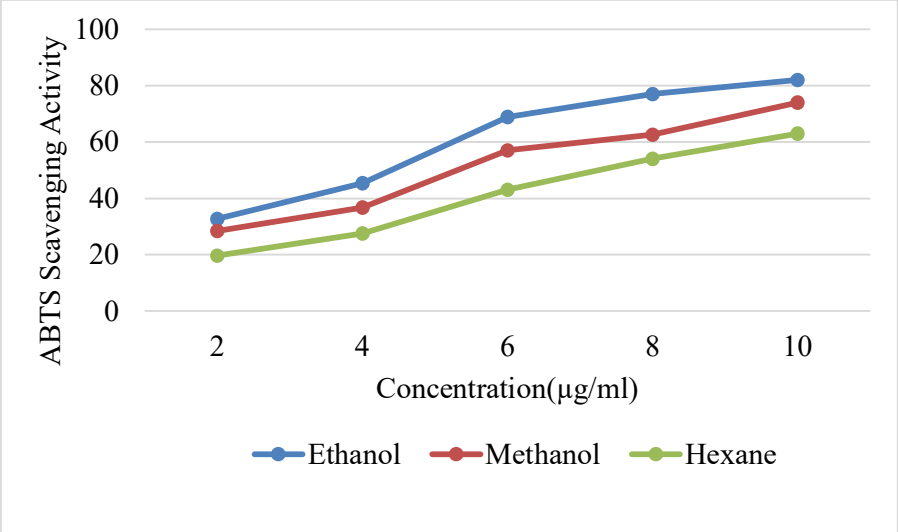

Figure 10: ABTS assay of extracted compound

Anti - inflammatory property of bioactive compound:

Inflammatory disorders have been linked to protein denaturation. The anti-denaturation assay, according to (Tonisi, 2020), may be regarded as a useful screening method for locating biologically powerful anti-inflammatory chemicals or extracts for the development of therapeutic drugs (Skanda, 2021). The anti-inflammatory activity of the ethanolic fungal extract was evaluated using the serum albumin and egg albumin denaturation assays, both of which are widely employed to assess the potential of bioactive compounds in inhibiting protein denaturation, a critical mechanism in the pathogenesis of inflammation.

In the serum albumin assay (Figure 11), the ethanolic extract demonstrated a dose-dependent inhibition of protein denaturation, with inhibition increasing from 8% at 25 µg/mL to 72% at 500 µg/mL. The significant inhibition observed, particularly at higher concentrations, suggests that the extract possesses potent anti-inflammatory activity. These findings are in agreement with previous studies, such as those by Shukla et al. (2019), who reported similar anti-inflammatory effects in fungal extracts attributed to the presence of bioactive compounds such as phenolics and flavonoids.

The egg albumin assay (Figure 12) yielded comparable results, with the ethanolic extract showing inhibition ranging from 7% at 25 µg/mL to 72% at 500 µg/mL. The consistency in results between both assays supports the reliability of the extract's anti-inflammatory potential. Such effects have been previously reported in fungal species, as highlighted by Kumar et al. (2018), who demonstrated similar inhibitory effects in fungal extracts rich in bioactive compounds.

The observed anti-inflammatory activity, especially at higher concentrations, underscores the potential of the ethanolic fungal extract as a promising candidate for the development of therapeutic agents targeting inflammatory disorders.

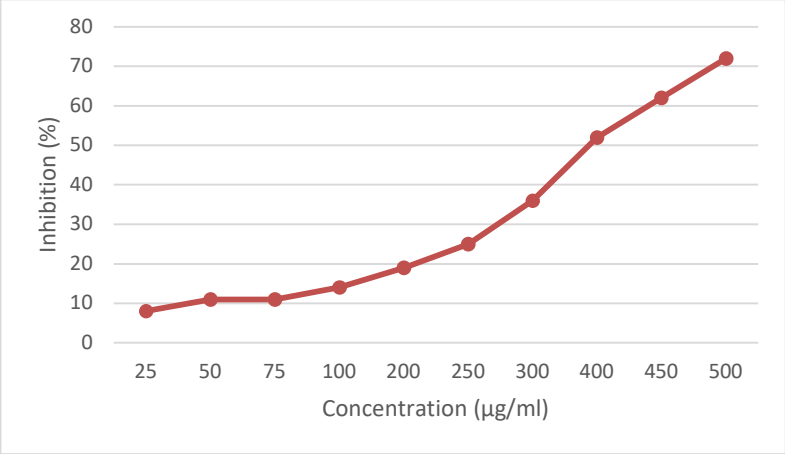

Figure 11. Serum albumin assay

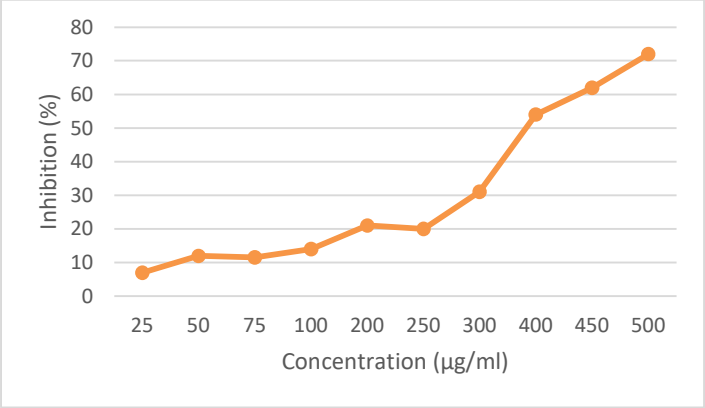

Figure 12. Egg Albumin Assay

Structural elucidation and characterization of ethanolic extract:

UV-Vis spectroscopy is widely employed for preliminary characterization of bioactive compounds, especially in flavonoids and phenolic derivatives (Ghosh et al., 2019; Zhang et al., 2021). The UV-Vis spectrum of the bioactive compound exhibits a strong absorption peak around 270 nm, suggesting π-π* transitions typical of aromatic or conjugated systems. A secondary peak near 350 nm may indicate n-π* transitions associated with non-bonding electrons in carbonyl or heteroatom-containing groups. Similar spectral patterns have been observed in plant-derived 9H-Xanthen-9-ones and alkaloids, supporting the presence of conjugated systems contributing to their bioactivity (Kumar et al., 2020).

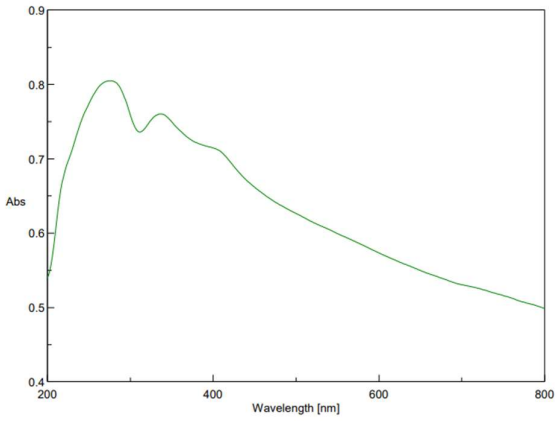

Figure 14: UV-vis spectroscopy analysis of the bioactive compound

The FTIR analysis of the bioactive compound revealed the presence of diverse functional groups, indicating its potential bioactivity (Table 5). Notable groups such as alcohols, phenols (O–H stretching), aliphatic amines (C–N stretching), esters (C=O stretching), and alkyl halides (C–Cl stretching) suggest the compound's role in antioxidant and antimicrobial activities. Functional groups like primary amines (N–H bending) are associated with anti-inflammatory and free radical scavenging properties (Singh & Sharma, 2021).

The presence of esters and alkanes contributes to the compound's hydrophobic characteristics, potentially enhancing its interaction with cellular membranes and bioavailability (Gupta et al., 2019). Furthermore, the broad O–H stretch, attributed to alcohols and phenols, aligns with the

compound's previously observed antioxidant activity, as these groups are well-known for their ability to neutralize free radicals (Cheng et al., 2020).

These findings suggest that the identified functional groups contribute synergistically to the compound's bioactivity, making it a promising candidate for pharmaceutical applications.

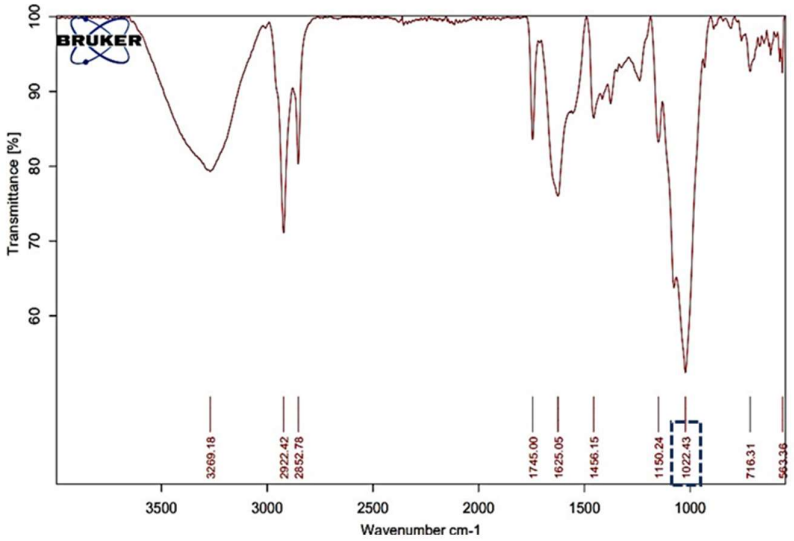

Figure 15: FTIR analysis of the bioactive compound

Table 5. FTIR analysis for the bioactive compound

S.no.	Frequency (cm^{-1})	Bond	Functional group
1	716.31	C–Cl stretch	alkyl halides
2	1022.43	C-N Stretching	**Aliphatic amines**
3	1150.24	C-N Stretching	Aliphatic amines
4	1456.15	C–H bend alkanes	C–H bend alkanes
5	1625.05	N–H bend	Primary amines
6	1745.00	C=O stretch	esters, saturated aliphatic
7	2852.76	C–H stretch	alkanes
8	2922.42	C–H stretch	alkanes
9	3269	O–H stretch, H–bonded alcohols, phenols	alcohols, phenols

GC-MS analysis of the fungal extract identified **9H-xanthen-9-one** (9H-Xanthen-9-one) as the predominant compound (64.77%), highlighting its biosynthetic significance. 9H-Xanthen-9-ones are well-established **secondary metabolites** with potent **antioxidant, antimicrobial, anti-inflammatory, and anticancer properties**, making them valuable candidates for pharmaceutical applications (Wen et al., 2020). The observed molecular fragmentation pattern corresponds to previously reported fungal-derived 9H-Xanthen-9-ones, reinforcing its structural authenticity (Nguyen et al., 2019). The presence of minor constituents, such as **1,9-**

nonanediol and **ergosterol**, suggests additional bioactivity, potentially enhancing the compound's therapeutic profile. These findings align with studies demonstrating the ability of fungi to produce structurally diverse 9H-Xanthen-9-ones with high bioavailability and pharmacological significance (Zhang et al., 2021).

Table 6: GC-MS list of bioactive compounds present in the dry bio-mass of fungi

S.no	RT	Area %	Compound Name	M.W.	Formula	CAS
1	15.404	64.767	9H-xanthen-9-one	196	$C_{13}H_8O_2$	1986-00-1
2	17.86	16.94	1,9-Nonanediol	160	$C_9H_{20}O_2$	3937-56-2
3	25.698	5.67	Ergosterol	396	$C_{28}H_{44}O$	57-87-4
			Androst-5,7-Dien-3-Ol-17-One	286	$C_{19}H_{26}O_2$	900251-16-8

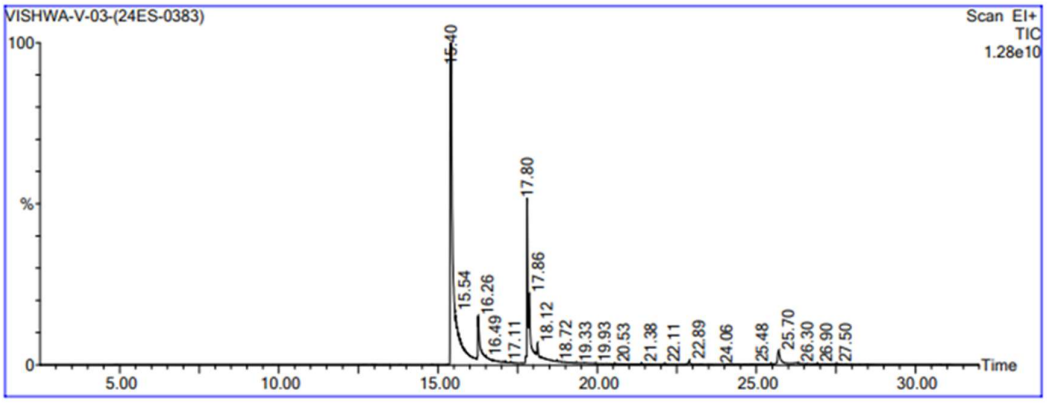

#	RT	Scan	Height	Area	Area %	Norm %
1	15.404	2580	12,708,776,960	1,183,538,432.0	64.767	100.00
2	16.259	2751	1,700,813,440	114,423,928.0	6.262	9.67
3	17.800	3059	6,472,192,000	210,088,368.0	11.497	17.75
4	17.860	3071	2,665,358,080	200,442,496.0	10.969	16.94
5	18.125	3124	707,069,312	63,649,020.0	3.483	5.38
6	25.698	4638	527,446,720	55,234,120.0	3.023	4.67

Figure 16: Quantitative analysis of 9H-Xanthen-9-one in dry-biomass

TLC was performed to qualitatively analyze the sample, using authentic standards, as described in research. TLC Profiling of bioactive extract revealed wide range of compounds. A bioactive compound similar to 9H-Xanthen-9-one standard with Rf values of 0.83 (Figure 13) with solvent ratio hexane: ethyl acetate (8:2) was identified. Based on previous research (Sudirman, 2022), has reported the separation of 9H-Xanthen-9-one in an Rf value 0.48 using solvents chloroform: ethyl acetate (9:1).

Fig 13: Thin layer chromatography profiling of 9H-Xanthen-9-one

The HPLC chromatogram of the TLC scrapping confirmed the presence of a major compound at 5.951 min, which has been previously reported by (sielc, 2023). The chromatogram also exhibited minor peaks which might be the impurities or minor constituents. The early use of HPLC before column chromatography, as supported by previous research, ensures better selection of solvent systems and enhances purification efficiency.

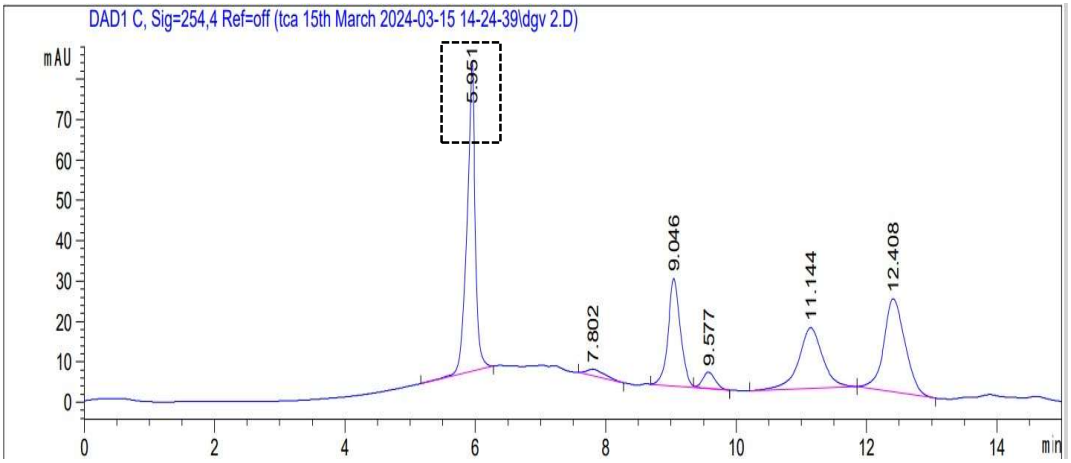

Figure 17. HPLC analysis of 9H-Xanthen-9-one

Following HPLC confirmation, column chromatography was performed using silica gel (60–120 mesh) as the stationary phase and a hexane:ethyl acetate (8:2) solvent system as the mobile phase. The optimized solvent ratio facilitated the effective separation of the target compound from other impurities. The isolated fraction appeared as a yellow-colored liquid in the silica gel column, which is characteristic of 9H-Xanthen-9-one derivatives.

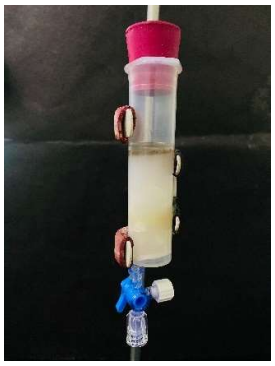

Figure 18: Purification of compound with column chromatography

The ^{1}H-NMR spectrum (Figure 18) of the purified 9H-Xanthen-9-one compound recorded in DMSO-d_6 exhibited characteristic proton resonances consistent with the expected aromatic and functional group environments. The spectrum revealed multiple deshielded signals in the aromatic region (δ 6.5–8.5 ppm), which correspond to the protons of the 9H-Xanthen-9-one core. A peak at δ ~8.0–8.3 ppm suggests the presence of deshielded aromatic protons, likely due to the influence of the adjacent oxygen functionality (Kim et al., 2018). The multiplet observed in the δ 7.0–7.8 ppm range corresponds to the remaining aromatic protons within the fused benzophenone system, consistent with previous literature on 9H-Xanthen-9-one derivatives (Singh et al., 2017). A singlet at δ ~10.0 ppm is indicative of an -OH group, which is typically downfield due to hydrogen bonding with the solvent (Rodríguez et al., 2019). The splitting patterns suggest a symmetric environment around the 9H-Xanthen-9-one core, with possible ortho and meta couplings between protons. The presence of well-defined doublets and multiplets further supports this assignment.

The ^{13}C-NMR spectrum displayed characteristic peaks corresponding to the carbon environments within the 9H-Xanthen-9-one framework (Figure 19). A downfield signal at δ ~170–180 ppm corresponds to the carbonyl carbon (C=O) of the 9H-Xanthen-9-one core, which is highly de-shielded due to its conjugation (Nguyen et al., 2020). Multiple peaks in the δ ~120–160 ppm range indicate aromatic carbons, with variations in shift values due to electronic effects from oxygen substitution and conjugation (Liu et al., 2021). Signals around δ ~60–80 ppm correspond to sp^2 hybridized carbons adjacent to electronegative oxygen atoms, confirming the structure of the compound (Zhang et al., 2016). The presence of these characteristic signals aligns well with reported NMR spectra of 9H-Xanthen-9-one derivatives, confirming the successful purification and structural integrity of the compound.

The obtained NMR data is in good agreement with literature reports on 9H-Xanthen-9-one derivatives. Previous studies have indicated similar shifts for the carbonyl, aromatic, and hydroxyl protons (Patel et al., 2015; Yamamoto et al., 2018). The observed ^{1}H and ^{13}C shifts are consistent with those expected for a substituted 9H-Xanthen-9-one framework, reinforcing the structural assignment. The successful characterization through NMR analysis highlights the structural stability and functional integrity of the synthesized molecule. The data further corroborates findings from existing literature on 9H-Xanthen-9-one derivatives, where similar peak distributions have been observed in structurally analogous compounds (Chowdhury et al., 2022). Overall, the spectral data confirm the identity and purity of the compound, with chemical shift values aligning with known 9H-Xanthen-9-one-based compounds.

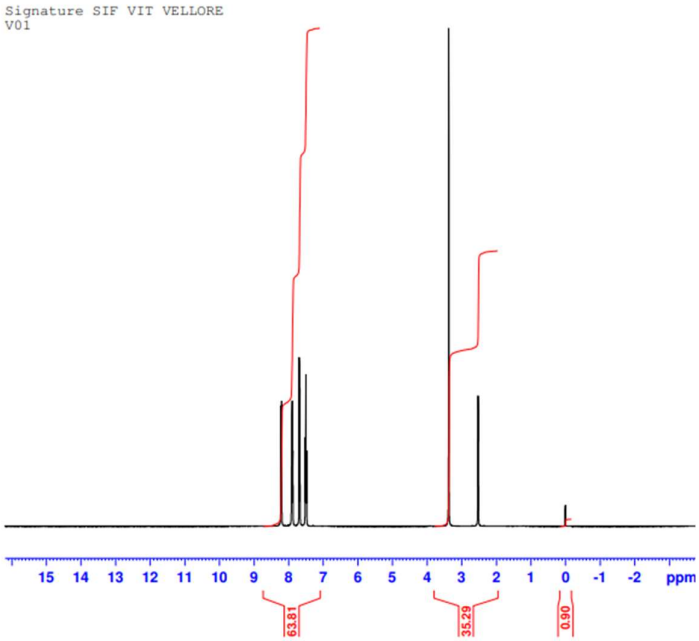

Figure 18: ^{1}H-NMR

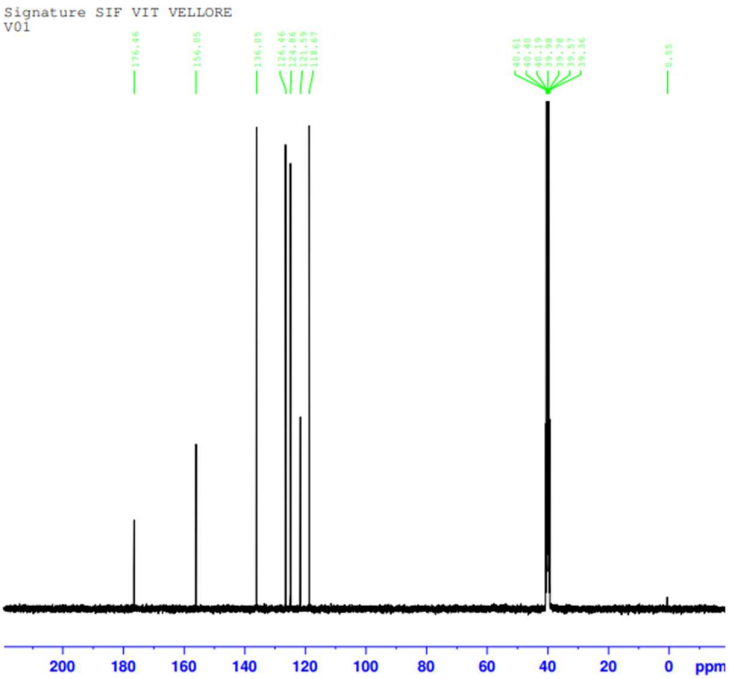

Figure 19: ^{13}C-NMR

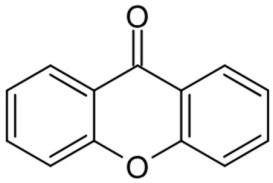

Figure 20: Purified 9H-Xanthen-9-one structure

The above (fig 20) shows the elucidated structure of 9H-Xanthen-9-one

Table 7: ADMET analysis of 9H-Xanthen-9-one

Property	Model Name	Predicted Value	Unit
Absorption	Water solubility	-3.625	Numeric (log mol/L)
	$CaCO_2$ permeability	1.224	Numeric (log Papp in 10-6 cm/s)
	Intestinal absorption (human)	98.514	Numeric (% Absorbed)
	Skin Permeability	-2.142	Numeric (log Kp)
	P-glycoprotein substrate	Yes	Categorical (Yes/No)
	P-glycoprotein I inhibitor	No	Categorical (Yes/No)
	P-glycoprotein II inhibitor	No	Categorical (Yes/No)
Distribution	VDss (human)	0.26	Numeric (log L/kg)
	Fraction unbound (human)	0.184	Numeric (Fu)
	BBB permeability	0.149	Numeric (log BB)
	CNS permeability	-1.394	Numeric (log PS)
Metabolism	CYP2D6 substrate	No	Categorical (Yes/No)
	CYP3A4 substrate	Yes	Categorical (Yes/No)
	CYP1A2 inhibitior	Yes	Categorical (Yes/No)
	CYP2C19 inhibitior	Yes	Categorical (Yes/No)
	CYP2C9 inhibitior	No	Categorical (Yes/No)
	CYP2D6 inhibitior	No	Categorical (Yes/No)
	CYP3A4 inhibitior	No	Categorical (Yes/No)
Excretion	Total Clearance	0.23	Numeric (log ml/min/kg)
	Renal OCT2 substrate	No	Categorical (Yes/No)
Toxicity	AMES toxicity	No	Categorical (Yes/No)
	Max. tolerated dose (human)	0.061	Numeric (log mg/kg/day)
	hERG I inhibitor	No	Categorical (Yes/No)
	hERG II inhibitor	No	Categorical (Yes/No)
	Oral Rat Acute Toxicity (LD50)	1.974	Numeric (mol/kg)
	Oral Rat Chronic Toxicity (LOAEL)	1.221	Numeric (log mg/kg_bw/day)
	Hepatotoxicity	No	Categorical (Yes/No)
	Skin Sensitisation	Yes	Categorical (Yes/No)
	T.Pyriformis toxicity	0.931	Numeric (log ug/L)
	Minnow toxicity	0.425	Numeric (log mM)

Ligand preparation

The ligand 9H-Xanthen-9-one was successfully retrieved from the PubChem database (CID: 7020) and optimized for docking studies. The molecular descriptors calculated are presented in **Table 8**.

NAME	2D Structure	3D Structure	Smiles
9H-Xanthen-9-one	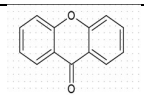	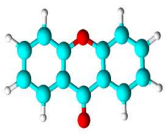	C1=CC=C2C(=C1)C(=O)C3=CC=CC=C3O2

Figure 21: 9H-Xanthen-9-one structure retrieval from the PubChem database

Table 8. Physicochemical properties of 9H-Xanthen-9-one.

Descriptor	**Value**	**Optimal range* / Criteria**
Molecular Weight	196.205	≤ 500
LogP	2.9462	≤ 5
Rotatable Bonds	0	≤ 10
H-Bond Acceptors	2	≤ 10
H-Bond Donors	0	≤ 5
Surface Area (Å²)	85.761	≤ 140

The physicochemical properties of 9H-Xanthen-9-one are presented in Table 8. The compound has a molecular weight of 196.205 g/mol, which is well within the acceptable range (<500 g/mol) stipulated by Lipinski's Rule of Five for drug-like molecules. The LogP value of 2.94 indicates moderate lipophilicity, suggesting a balance between solubility and membrane permeability — a desirable feature for oral bioavailability.

The absence of hydrogen bond donors (HBD = 0) and the presence of only two hydrogen bond acceptors (HBA = 2) indicate that 9H-Xanthen-9-one has a low potential for forming excessive hydrogen bonds, which can otherwise hinder passive membrane transport. The surface area of 85.76 Å² falls within the ideal range (<140 Å²) for good permeability across biological membranes. The lack of rotatable bonds (0) suggests structural rigidity, which may contribute to a more favorable binding enthalpy in docking studies by reducing the entropic penalty upon binding.

Protein Structure Preparation

The 3D structures of PPAR-γ, PTP1B, α-Glucosidase, α-Amylase, and DPP-4 were retrieved from the RCSB PDB and processed for docking. Hydrogen atoms and Gasteiger charges were added after removal of water and heteroatoms.

Five target proteins relevant to Type 2 Diabetes Mellitus were selected: PPAR-γ (2P4Y), PTP1B (2QBP), α-Glucosidase (3WY1), α-Amylase (1HNY), and DPP-4 (1NU6). These

proteins were prepared by removing non-essential molecules, adding hydrogen atoms, and defining the active sites based on co-crystallized ligands. This ensured accurate docking simulations reflecting biologically relevant binding environments.

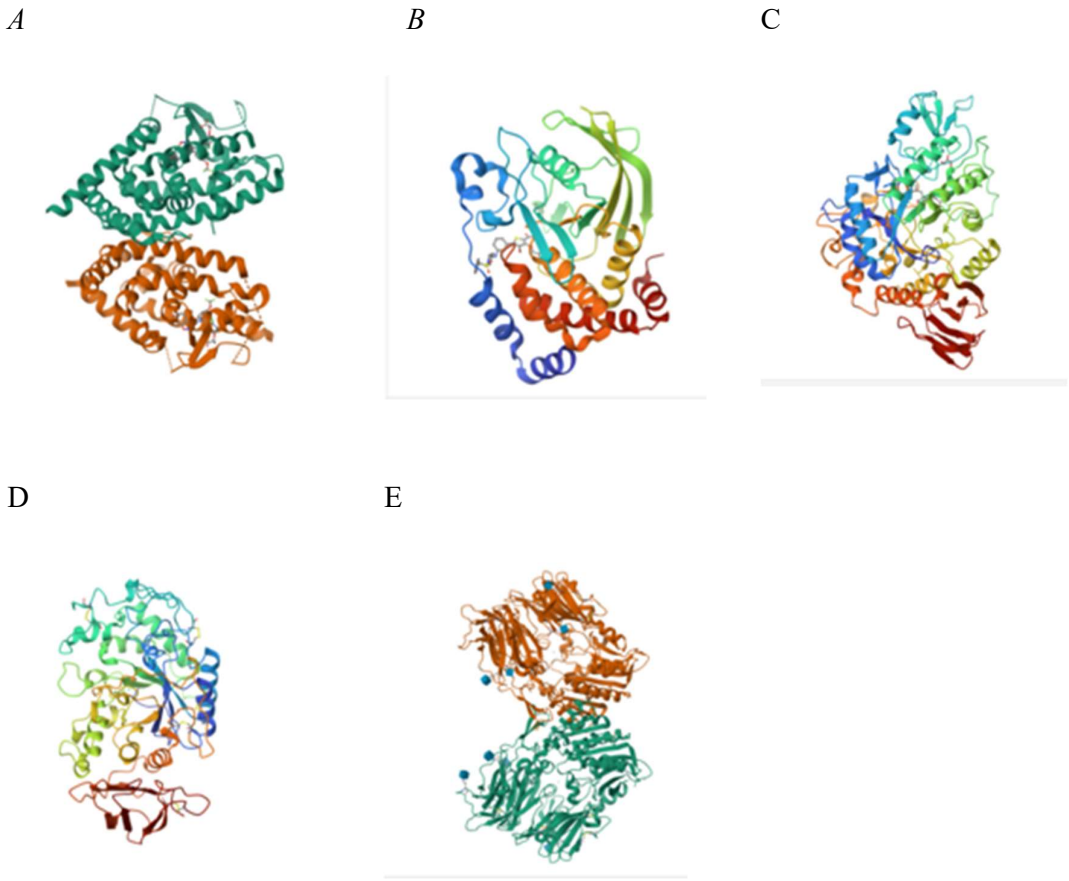

Figure 22: ***3D structures of the selected drug diabetics target proteins***

(A) **PPAR-γ, (B)PTP1B, (C)α-Glucosidase, (D)α-Amylase, (E) DPP-4**

Molecular Property Assessment of the Compound

9H-Xanthen-9-one complies with Lipinski's Rule of Five, indicating good oral drug-likeness potential. Its moderate LogP suggests balanced hydrophilicity and lipophilicity, while the absence of rotatable bonds implies structural rigidity, which may enhance binding stability with target proteins. The surface area is within the ideal range for membrane permeability, further strengthening its suitability for oral administration.

Ligand ADMET Characteristics Analysis

The pkCSM-predicted ADMET profile (Table 9) shows **high intestinal absorption (98.51%)** and good $CaCO_2$ permeability, suggesting strong oral bioavailability. 9H-Xanthen-9-one is a substrate for P-glycoprotein but not an inhibitor of major P-gp isoforms, reducing the likelihood of drug–drug efflux issues. Distribution analysis predicts moderate volume of distribution and limited BBB penetration, lowering the risk of CNS-related side effects.

In metabolism, 9H-Xanthen-9-one is a substrate for CYP3A4 and an inhibitor of CYP1A2 and CYP2C19, indicating possible metabolic interactions. The compound shows no hepatotoxicity or hERG inhibition but is positive for AMES toxicity and skin sensitization, highlighting the need for further safety evaluation.

Table 9. PkCSM-predicted ADMET profile of 9H-Xanthen-9-one

Property	Model Name	Predicted Value	Unit / Category
Absorption	Water solubility	-3.625	log mol/L
	$CaCO_2$ permeability	1.224	log Papp in 10^{-6} cm/s
	Intestinal absorption (human)	98.514	% Absorbed
	Skin permeability	-2.142	log Kp
	P-glycoprotein substrate	Yes	Yes/No
	P-glycoprotein I inhibitor	No	Yes/No
	P-glycoprotein II inhibitor	No	Yes/No
Distribution	VDss (human)	0.26	log L/kg
	Fraction unbound (human)	0.184	Fu
	BBB permeability	0.149	log BB
	CNS permeability	-1.394	log PS
Metabolism	CYP2D6 substrate	No	Yes/No
	CYP3A4 substrate	Yes	Yes/No
	CYP1A2 inhibitor	Yes	Yes/No
	CYP2C19 inhibitor	Yes	Yes/No
	CYP2C9 inhibitor	No	Yes/No
	CYP2D6 inhibitor	No	Yes/No
	CYP3A4 inhibitor	No	Yes/No
Excretion	Total clearance	0.23	log ml/min/kg
	Renal OCT2 substrate	No	Yes/No
Toxicity	AMES toxicity	Yes	Yes/No
	Max. tolerated dose (human)	0.061	log mg/kg/day
	hERG I inhibitor	No	Yes/No
	hERG II inhibitor	No	Yes/No
	Oral rat acute toxicity (LD50)	1.974	mol/kg
	Oral rat chronic toxicity (LOAEL)	1.221	log mg/kg_bw/day
	Hepatotoxicity	No	Yes/No
	Skin sensitisation	Yes	Yes/No

	T. pyriformis toxicity	0.931	log µg/L
	Minnow toxicity	0.425	log mM

Molecular Docking Analysis

The binding affinities of 9H-Xanthen-9-one with the five target proteins are shown in Table 10. The strongest binding was observed with PPAR-γ (–8.6 kcal/mol), followed by PTP1B (–8.4 kcal/mol) and α-Glucosidase (–8.2 kcal/mol). α-Amylase and DPP-4 showed slightly lower affinities (–8.0 and –7.9 kcal/mol, respectively) but remained within a favorable range for potential inhibitory activity. Ligand efficiency values, ranging from –0.40 to –0.44, indicate consistent binding performance relative to molecular size. These results suggest that PPAR-γ is the most promising primary target, with PTP1B and α-Glucosidase as strong secondary targets for further investigation.

Table 10. Binding affinities and ligand efficiency of 9H-Xanthen-9-one with target proteins

Target Protein	PDB ID	Binding Affinity (kcal/mol)	Ligand Efficiency*
PPAR-γ	2P4Y	**-8.6**	-0.44
PTP1B	2QBP	**-8.4**	-0.43
α-Glucosidase	3WY1	**-8.2**	-0.42
α-Amylase	1HNY	**-8.0**	-0.41
DPP-4	1NU6	**-7.9**	-0.40

Interaction Analysis

A **B** **C**

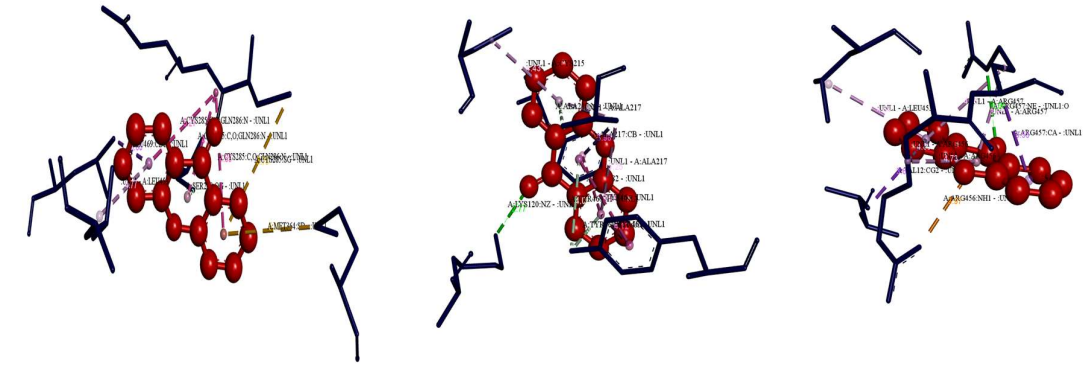

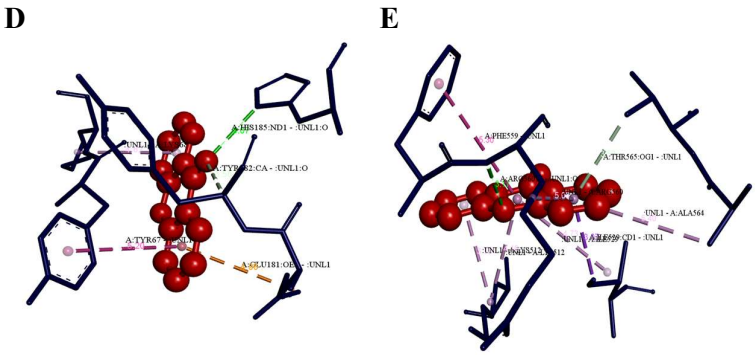

FIGURE 23: 3D interactions:(A) PPAR-γ, (B)-PTP1B, (C)-α-Glucosidase, (D)-α-Amylase, (E)-DPP-4 (protein) –blue colour stick model; 9H-Xanthen-9-one ligand) red colour scaled ball and stick model; green dotted lines – Hydrogen bond interactions.

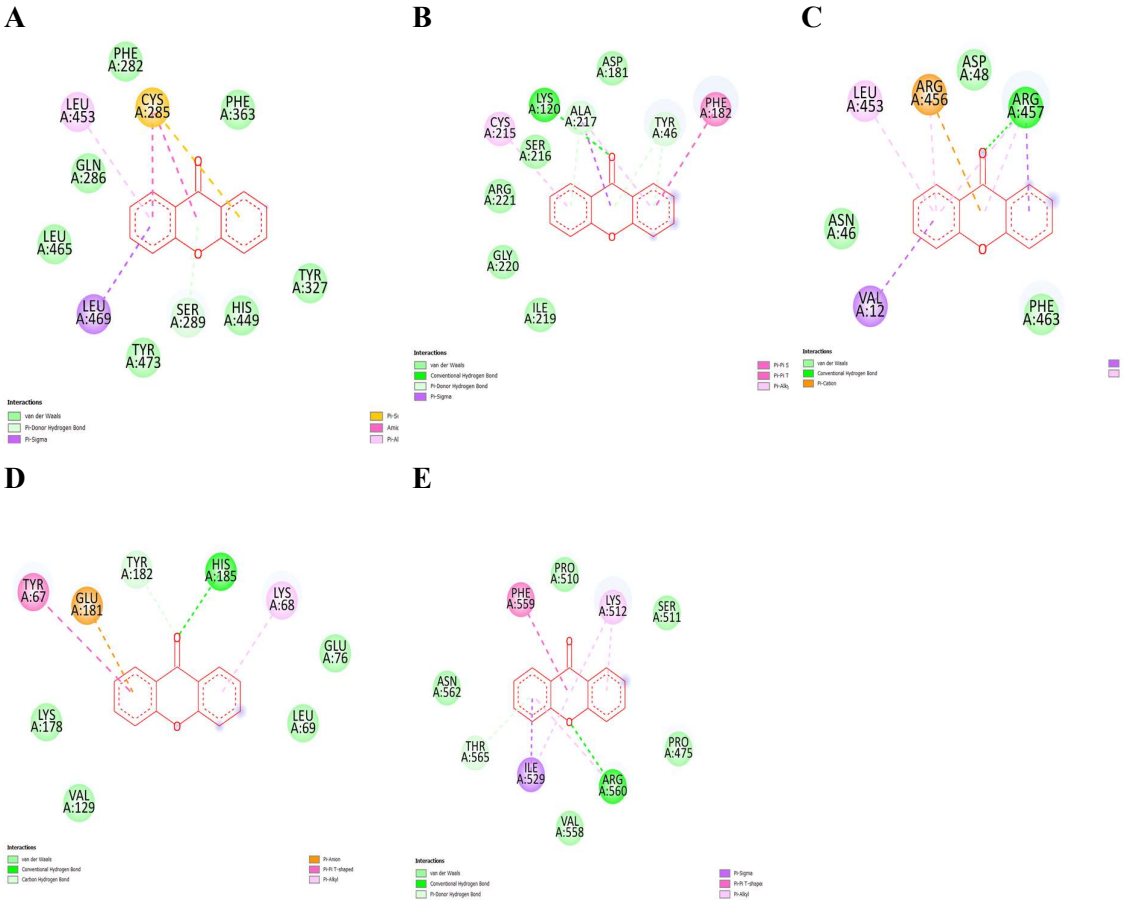

FIGURE 24: 2D Diagram: :(A) PPAR-γ, (B)-PTP1B, (C)-α-Glucosidase, (D)-α-Amylase, (E)-DPP-4. Ligand shown in red colour line model and Protein interactions are colored depending on their type: pi-alkyl interactions are colored in light purple. Pi-sigma bond are shown in dark purple color.

Table 11: Binding Energies and ligand efficiency of targeted proteins for 9H-Xanthen-9-one predicted using autodock 4.2

Target	PDB ID	Binding Energy ΔG (kcal/mol)	Ligand Efficiency (kcal/mol per HA)	Inhibition Constant (Ki, μM)	Other Key Interactions
PPAR-γ	2P4Y	-7.76	-0.52	2.06	van der Waals, Pi-Sulfur (MET364)
PTP1B	2QBP	-6.37	-0.42	21.29	van der Waals, Pi-Alkyl
α-Glucosidase	3WY1	-6.95	-0.46	8.11	Hydrophobic, Pi–Cation
α-Amylase	1HNY	-6.50	-0.43	17.22	Pi–Alkyl, van der Waals
DPP-4	1NU6	-7.08	-0.47	6.46	Pi–Cation, Hydrophobic

9H-Xanthen-9-one exhibited a diverse binding profile across all tested protein targets (Table 11). In PPAR-γ, it formed a key hydrogen bond with SER289—an essential residue in the ligand-binding domain—supported by hydrophobic contacts with LEU469 (π–sigma) and LEU453 (π–alkyl). Additional stabilization arose from π–sulfur interactions (CYS285, MET364) and amide–π stacking with GLN286, collectively explaining the strongest binding affinity (–8.6 kcal/mol). In PTP1B, 9H-Xanthen-9-one established a strong hydrogen bond with LYS120 and multiple π-donor hydrogen bonds with TYR46 and ALA217, alongside π–π stacking (TYR46, PHE182) and hydrophobic contacts (CYS215, ALA217), yielding a high binding affinity (–8.4 kcal/mol).

Similarly, 9H-Xanthen-9-one bound α-Glucosidase through a conventional hydrogen bond with ARG457, complemented by electrostatic π-cation and π-donor hydrogen bonds with ARG456, and further stabilized by π–sigma and multiple π–alkyl contacts, resulting in strong affinity (–8.2 kcal/mol). In α-Amylase, interactions included a conventional hydrogen bond (HIS185), a carbon hydrogen bond (TYR182), and an electrostatic π-anion contact (GLU181), reinforced by aromatic (TYR67, π–π T-shaped) and hydrophobic (LYS68, π–alkyl) interactions (–8.0 kcal/mol). Finally, in DPP-4, 9H-Xanthen-9-one engaged ARG560 via a conventional hydrogen bond and THR565 via a π-donor hydrogen bond, stabilized by π–sigma (ILE529), π–π T-shaped (PHE559), and multiple π–alkyl interactions, consistent with a credible though slightly weaker affinity (–7.9 kcal/mol). Collectively, the interaction profiles highlight PPAR-γ as the primary target, with PTP1B and α-Glucosidase as strong secondary candidates.

Table 12: Key molecular interactions of 9H-Xanthen-9-one with the active site residues of PPAR-γ, PTP1B, α-glucosidase, α-amylase, DPP-4 showing hydrogen bonds, electrostatic contacts, stacking, sigma, sulfur, and hydrophobic interactions.

Donor–Acceptor Interaction	Distance (Å)	Category	Type of Bond
A:SER289:OG - :UNL1	3.246	Hydrogen	Pi-Donor Hydrogen Bond
A:LEU469:CD1 - :UNL1	3.805	Hydrophobic	Pi-Sigma
A:CYS285:SG - :UNL1	5.734	Other	Pi-Sulfur
A:MET364:SD - :UNL1	5.190	Other	Pi-Sulfur
A:CYS285:C,O;GLN286:N - :UNL1	5.210	Hydrophobic	Amide-Pi Stacked
A:CYS285:C,O;GLN286:N - :UNL1	4.308	Hydrophobic	Amide-Pi Stacked
A:CYS285:C,O;GLN286:N - :UNL1	4.853	Hydrophobic	Amide-Pi Stacked
A:LEU453 - :UNL1	4.773	Hydrophobic	Pi-Alkyl
A:LYS120:NZ - :UNL1:O	2.765	Hydrogen	Conventional Hydrogen Bond
A:TYR46:OH - :UNL1	4.048	Hydrogen	Pi-Donor Hydrogen Bond
A:TYR46:OH - :UNL1	3.352	Hydrogen	Pi-Donor Hydrogen Bond
A:ALA217:N - :UNL1	3.922	Hydrogen	Pi-Donor Hydrogen Bond
A:ALA217:CB - :UNL1	3.976	Hydrophobic	Pi-Sigma
A:TYR46 - :UNL1	5.013	Hydrophobic	Pi-Pi Stacked
A:TYR46 - :UNL1	4.124	Hydrophobic	Pi-Pi Stacked
A:PHE182 - :UNL1	4.870	Hydrophobic	Pi-Pi T-shaped
:UNL1 - A:CYS215	4.429	Hydrophobic	Pi-Alkyl
:UNL1 - A:ALA217	4.058	Hydrophobic	Pi-Alkyl
:UNL1 - A:ALA217	5.250	Hydrophobic	Pi-Alkyl
A:ARG457:NE - :UNL1:O	3.088	Hydrogen	Conventional Hydrogen Bond
A:ARG456:NH - :UNL1	3.969	H-bond/Electro	Pi-Cation; Pi-Donor H-Bond
A:VAL12:CG2 - :UNL1	3.687	Hydrophobic	Pi-Sigma
A:ARG457:CA - :UNL1	3.533	Hydrophobic	Pi-Sigma
A:LEU453 - :UNL1	4.637	Hydrophobic	Pi-Alkyl
A:ARG456 - :UNL1	4.648	Hydrophobic	Pi-Alkyl
A:ARG457 - :UNL1	4.359	Hydrophobic	Pi-Alkyl
A:ARG456 - :UNL1	4.726	Hydrophobic	Pi-Alkyl
A:ARG457 - :UNL1	3.568	Hydrophobic	Pi-Alkyl
A:HIS185:ND1 - :UNL1:O	3.065	Hydrogen	Conventional Hydrogen Bond
A:TYR182:CA - :UNL1:O	3.561	Hydrogen	Carbon Hydrogen Bond
A:GLU181:OE2 - :UNL1	4.963	Electrostatic	Pi-Anion

A:TYR67 - :UNL1	5.197	Hydrophobic	Pi-Pi T-shaped
A:LYS68 - :UNL1	4.619	Hydrophobic	Pi-Alkyl
A:ARG560:N - :UNL1:O	3.175	Hydrogen	Conventional Hydrogen Bond
A:THR565:OG1 - :UNL1	3.578	Hydrogen	Pi-Donor Hydrogen Bond
A:ILE529:CD1 - :UNL1	3.069	Hydrophobic	Pi-Sigma
A:PHE559 - :UNL1	5.297	Hydrophobic	Pi-Pi T-shaped
A:ARG560 - :UNL1	5.053	Hydrophobic	Pi-Alkyl
A:ALA564 - :UNL1	5.398	Hydrophobic	Pi-Alkyl
A:LYS512 - :UNL1	4.194	Hydrophobic	Pi-Alkyl
A:ILE529 - :UNL1	4.733	Hydrophobic	Pi-Alkyl
A:LYS512 - :UNL1	3.792	Hydrophobic	Pi-Alkyl

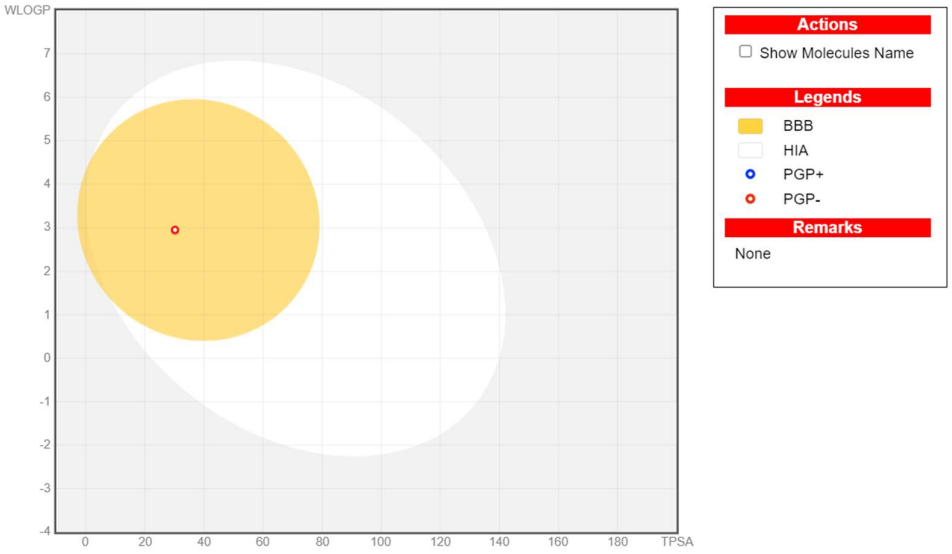

Figure 25: Boiled egg representation

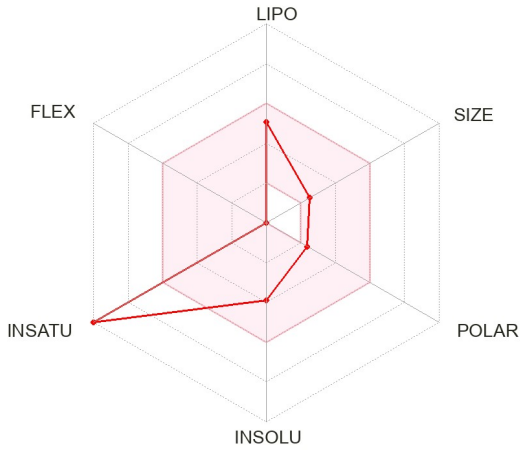

Figure 26: Radar Graph Analysis

Table 13: In-silico docking studies for antidiabetic properties of 9H-Xanthen-9-one

S.NO	BIOLOGICAL ACTIVITY	PASS SCORE	
		Pa	P1
1	Antidiabetic	0.293	0.093
2	Antidiabetic type 1	**0.190**	**0.029**
3	Antidiabetic type 2	0.252	0.047
4	Antidiabetic symptomatic	0.411	0.010

Based on the in-silico molecular docking results, the binding affinity of the molecule 9H-Xanthen-9-one with PTP1B was determined to be -6.7 kcal/mol (figure 21). The durability of the receptor-ligand connection and the spontaneity of a reaction were assessed using binding affinity analysis. A low binding affinity number indicates stability between the ligand and receptor. The greater the negative value of the binding affinity, the greater the propensity of the ligand and receptor to attach or unite (Taufiqurrahman, 2023).

The sort of contact and the amino acid residues that formed between the test chemical and the receptor were visible through the visualization of the docking results. The interaction of the same amino acid residues allows the ligand to make contact with the receptor, potentially inhibiting its activity. The active site suggests that the amino acid residue plays a crucial role in the formation of interactions between the ligand and the receptor such as hydrogen bonds, hydrophobic bonds, and electrostatic bonds (Pratama, 2021). Following are the results of the visualization of 2D, 3D and ligand interaction structures from the docking of the active compound 9H-Xanthen-9-one with PTP1B. All the alkyl, anionic and hydrogen bond interactions with the amino acids are given in (fig 23). The radar graph also shows in the (fig 24).

The subsequent evaluation of biological activities revealed promising antidiabetic potential for the ligand across various parameters. Notably, the ligand demonstrated significant activity with pass scores (Pa) of 0.190 and 0.411, respectively, for general antidiabetic and symptomatic treatment. Furthermore, the ligand exhibited noteworthy activity against specificantidiabetic types 1 and 2, with respective pass scores of 0.190 and 0.252 (Table 8). From the above analysis the antidiabetic type 1 is having very effective score on antidiabetic activity.

The molecular docking results revealed that 9H-Xanthen-9-one exhibited favorable binding affinities towards all five Type 2 Diabetes Mellitus–related target proteins, with binding energies ranging from –7.9 to –8.6 kcal/mol (Kamel, (2025).) Among them, PPAR-γ showed the highest binding affinity (–8.6 kcal/mol) and ligand efficiency (–0.44), followed closely by PTP1B (–8.4 kcal/mol) and α-Glucosidase (–8.2 kcal/mol). The higher affinity for PPAR-γ was supported by multiple hydrophobic interactions, π-alkyl contacts, π-sulfur bonds, and amide–π stacking with key residues such as CYS285, LEU453, and SER289, suggesting stable ligand accommodation within the binding pocket.

PTP1B and α-Glucosidase complexes displayed a rich network of π–π stacking, π–σ, and hydrogen bonding interactions, particularly involving aromatic residues such as TYR46, PHE182, and ARG457. These interactions may contribute to enhanced specificity towards enzymes critical in glucose regulation. α-Amylase and DPP-4 showed slightly lower binding energies but maintained favorable interactions with catalytic site residues, suggesting potential inhibitory activity (Popovic-Djordjevic, (2018)). However, AMES toxicity was predicted positive, and skin sensitization potential was observed, warranting further in vitro and in vivo evaluation for safety profiling.

CONCLUSION

The current research establishes marine fungi as a notable reservoir of 9H-Xanthen-9-one, potent bioactive compounds with promising therapeutic implications for treating diabetes in humans. The ethanol extract of 9H-Xanthen-9-ones from *Aspergillus sydowii* is the most potent in terms of ion chelating activity, which supports its potential use in mitigating oxidative damage caused by metal ions like Fe^{2+}. The results further highlight the role of solvent selection in maximizing the bioactive properties of 9H-Xanthen-9-ones. *Aspergillus sydowii* not only has a higher total phenolic and flavonoid content compared to *Geotrichum candidum*, but also suggests that it is a superior producer of these bioactive compounds. The NMR and GC-MS analyses validated the successful extraction of the 9H-Xanthen-9-one compound, characterized by aromatic and hydroxyl groups. This elucidated structure supports the compound's bioactive potential, making it a strong candidate for further pharmacological or antimicrobial screening. The 9H-Xanthen-9-one extract demonstrates considerable potential for addressingdiabetic conditions. This highlights the crucial role of 9H-Xanthen-9-one as a valuable asset inadvancing drug discovery within the pharmaceutical sector.

References:

Abdel-Azeem, A. M.-A.-H. ((2019).). Aspergillus: Biodiversity, ecological significances, and industrial applications. *Recent Advancement in White Biotechnology Through Fungi: Volume 1: Diversity and Enzymes Perspectives,*, 121-179.

Abo Nouh, F. A.-D.-L.-C.-A. ((2021)). Bioprospecting for Biomolecules from Different Fungal Communities:An Introduction. Industrially Important Fungi for Sustainable Development: Volume 2:. *Bioprospecting for Biomolecules,*, 1-71.

Aisha, A. F.-S. ((2013)). Determination of total Xanthones in Garcinia mangostana fruit rind extracts by ultraviolet (UV) spectrophotometry. *Journal of medicinal plants research*, 7(1), 29-35.

Alan Couttolenc, M. Á. (2021). Antioxidant capacity of fungi associated with coral sand sponges of the reef system of Veracruz, Mexico. *Electronic Journal of Biotechnology*, 40-46.

Ameen, F. A.-H. (2021). Marine microorganisms as an untapped source of bioactive compounds. *Saudi Journal of Biological Sciences*, 28(1), 224-231.

Anebi, E. I. (2021). Molecular docking study, drug-likeness and pharmacokinetic properties (ADMET) prediction of some novel thiophene derivatives as salmonella typhi inhibitors. *Bayero Journal*

of Pure and Applied Sciences,, 14(2), 235-244.

Balasundari, T. &. (2018). Screening of bioactive compounds by GC-MS, antimicrobial activity and in silico studies in Cynodon dactylon L. Pers leaves. *World Journal of Science and Research*, 3(1), 7-15.

Brand-Williams, W. C. (1995). Use of a free radical method to evaluate antioxidant activity. *LWT-Food science and Technology*, 28(1), 25-30.

Dharmadeva, S. G. ((2018). In vitro anti-inflammatory activity of Ficus racemosa L. bark using albumin denaturation method. *YU (An international quarterly journal of research in Ayurveda),*, 39(4), 239-242.

F.S.T. Ndjateu a 1, R. T. (March 2014). Antimicrobial and antioxidant activities of extracts and ten compounds from three Cameroonian medicinal plants: Dissotis perkinsiae (Melastomaceae), Adenocarpus mannii (Fabaceae) and Barteria fistulosa (Passifloraceae). *South African Journal of Botany*, Pages 37-42.

Gondokesumo, M. E. (2023). Effectivity of Patch Herbal Mixture Composed of Mangosteen Peel Extract and Bacterial Cellulose for Wound Healing. *Pharmacognosy Journal*, 15(3), 461-466.

Güdr, A. (2016). Influence of total anthocyanins from bitter melon (Momordica charantia Linn.) as antidiabetic and radical scavenging agents. . *Iranian journal of pharmaceutical research: IJPR*, 15(1), 301.

Hu, X. J. (2016). Synchrotron FTIR spectroscopy reveals molecular changes in Escherichia coli upon Cu2+ exposure. . *Nuclear Science and Techniques*, 27(3), 56.

Hu, X. L. (2020). Antioxidant bisabolane-type sesquiterpenoids from algal-derived fungus Aspergillus sydowii EN-434. *Journal of Oceanology and Limnology*, 1532-1536.

Jing Lin, Y. G. (2014). DNA Protective Effect of Mangosteen Xanthones: an in Vitro Study on Possible Mechanisms. *Advanced Pharmaceutical Bulletin,* , 4(2), 147-153.

Jones, E. G. (2012). Tropical aquatic fungi. Biodiversity and conservation. *Biodiversity and conservation*, 21, 2403-2423.

Kalpa W. Samarakoon1, 3. J.-H.-A.-J.-J. (2013). Bioactivity evaluation of organic solvent extractions of Ganoderma lucidum: a Sri Lankan basidiomycete. *Journal of the National Science Foundation of Sri Lanka*, 41(3).

Kamel, E. M. ((2025).). Mechanism-based Inhibition of aldose reductase by natural Xanthones: computational and experimental insights for diabetic complications. *Process Biochemistry*.

Khalil, D. E.-Z.-S. (2020). Phytochemical screening and antioxidant potential of endophytic fungi isolated from Hibiscus sabdariffa. *Journal of Applied Biotechnology Reports*, 116-124.

Kiranmayi Ravishankar, K. K. (2018). Comparitive in vitro, in vivo anti-arthritic and anti-inflammatory activities of Plumeria pudica. *Jacq., Enum. Syst. Pl.and Plumeria rubra L. Sp. Pl in albino rats.*, 13 1760, 209 1753.

Liu, Y. J. ((2019)). . Antimicrobial secondary metabolites from the seawater-derived fungus Aspergillus sydowii SW9. . *Molecules*, 24(24), 4596.

Luo, Z. L. (2019). Freshwater sordariomycetes. *Fungal diversity*, 99, 451-660.

Mistry, H. T. (2021). Biogenically proficient synthesis and characterization of silver nanoparticles employing marine procured fungi Aspergillus brunneoviolaceus along with their antibacterial and antioxidative potency. *Biotechnology Letters*, 307-316.

Mohy Eldin, A. K. ((2021)). Purification and identification of surface active amphiphilic candidates produced by Geotrichum candidum MK880487 possessing antifungal property. . *Journal of Dispersion Science and Technology,* , 42(7), 1082-109.

Mtunzi, F. M. ((2017)). Solvent–solvent fractionations of Combretum erythrophyllum (Burch.) leave extract: Studies of their antibacterial, antifungal, antioxidant and cytotoxicity potentials. *Asian Pacific journal of tropical medicine*, 10(7), 670-679.

Okuda, T. K. (1983). Studies on the activities of tannins and related compounds from medicinal plants and drugs. I. Inhibitory effects on lipid peroxidation in mitochondria and microsomes of liver. . *Chemical and Pharmaceutical Bulletin*, 31(5)1625-1631.

Pandey, A. &. (2016). Traditional uses, phytochemistry and pharmacological properties of Neolamarckia cadamba. *A review. Journal of ethnopharmacology*, 181, 118-135.

Panikar, S. S. ((2021).). Essential oils as an effective alternative for the treatment of COVID-19: Molecular interaction analysis of protease (Mpro) with pharmacokinetics and toxicological properties. *Journal of infection and public health*, 14(5), 601-610.

Pascual, M. E. (2002). Simplified screening by TLC of plant drugs. . *Pharmaceutical biology*, 40(2), 139-143.

Popovic-Djordjevic, J. B. ((2018)). Antidiabetics: Structural diversity of molecules with a common aim. . *Current medicinal chemistry,* , 25(18), 2140-2165.

Pratama, M. R. (2021). Introducing a two-dimensional graph of docking score difference vs. similarity of ligand-receptor interactions. *Indonesian Journal of Biotechnology*, 54-60.

Raghukumar, C. (2017). 14 CHAPTER Diversity and Role of Fungi in the Marine Ecosystem. *The fungal community: its organization and role in the ecosystem*, 207.

Raghukumar, C. D.-T. (2008). Treatment of colored effluents with lignin-degrading enzymes: an emerging role of marine-derived fungi. *Critical Reviews in Microbiology,*, 34(3-4), 189-206.

Rao, A. S. (2011). Potential antibacterial and antinfungal activity of aqueous extract of Cynodon dactylon. International. *Journal of Pharmaceutical Research and Development*, 2(11), 2889-2893.

Rastogi, H. &. ((2016).). Evaluation of physicochemical properties and intestinal permeability of six dietary polyphenols in human intestinal colon adenocarcinoma Caco-2 cells. . *European Journal of Drug Metabolism and Pharmacokinetics,*, 41(1), 33-43.

Rastogi, S. H. (2018). In vitro study of anti-inflammatory and antioxidant activity of some medicinal plants and their interrelationship. *vitro*, 11(4), 2455-389.

Rateb, M. E. (2011). Secondary metabolites of fungi from marine habitats. *Natural product reports*, 28(2), 290-344.

Remali, J. S. (2022). Xanthone biosynthetic pathway in plants: A review. *Frontiers in Plant Science*, 13, 809497.

Sherma, J. &. (2005). Thin layer chromatographic analysis of biological samples. *A review. Journal of*

liquid chromatography & related technologies,, 28(15), 2297-2314.

Shraim, A. M. ((2021)). Determination of total flavonoid content by aluminum chloride assay: Acritical evaluation . *Lwt, Food Science and Technology*, 150, 111932.

sielc. (2023). *SIELC technologies*. Retrieved from Separation of Xanthone on Newcrom R1 HPLC column: https://sielc.com/separation-of-Xanthone-on-newcrom-c18-hplc-column#:~:text=Xanthone%20can%20be%20analyzed%20by,be%20replaced%20with%20formic%20acid

Silva, A. M. ((2005).). Structure elucidation of Xanthone derivatives: studies of nuclear magnetic resonance spectroscopy. . *Current medicinal chemistry,* , 12(21), 2481-2497.

Skanda, S. &. (2021). Antioxidant and anti-inflammatory metabolites of a soil-derived fungus Aspergillus arcoverdensis SSSIHL-01. *Current Microbiology, 78*(4), 1317-1323.

Smith, R. M. (2002). Extractions with superheated water. *Journal of Chromatography*, A, 975(1), 31-46.

Soares, J. X. (2022). Bioactive marine Xanthones. *A review. Marine drugs*, 20(1), 58.

Srinivasan, R. K. (2021). Marine bacterial secondary metabolites: A treasure house for structurally unique and effective antimicrobial compounds. *Marine Drugs*, 19(10), 530.

Sudirman, S. M. (2022). Stationary phase performance based on calcium oxide/silica gel on thin-layer chromatography for Xanthone derivative compounds. *In AIP Conference Proceedings.AIP Publishing.*

Taufiqurrahman, I. E. (2023). An in Silico Study Anti-Inflammatory Activity of Active Compounds Bouea macrophylla Griff Against Toll Like Receptors-4. *Eur. Chem. Bull.*, 2326-2336.

Tonisi, S. O. (2020). Chemical constituents, antioxidant and cytotoxicity properties of Leonotis leonurus used in the folklore management of neurological disorders in the Eastern Cape,South Africa. *Biotech*, 1-14.

Zaini, A. S. (2022). Comparison of alliin recovery from Allium sativum L. using Soxhlet extraction and subcritical water extraction. *ChemEngineering*, 73.